



Characterisation of residual ionospheric errors in bending angles using GNSS RO end-to-end simulations

C.L. Liu^{a,b,*}, G. Kirchengast^c, K.F. Zhang^{a,b}, R. Norman^b, Y. Li^b, S.C. Zhang^b, B. Carter^b,
J. Fritzer^c, M. Schwaerz^c, S.L. Choy^b, S.Q. Wu^b, Z.X. Tan^a

^a Key Laboratory for Land Environment and Disaster Monitoring of SBSM, China University of Mining and Technology, Xuzhou 221116, China

^b SPACE Research Centre, RMIT University, VIC 3001, Australia

^c Wegener Center for Climate and Global Change and Institute for Geophysics, Astrophysics, and Meteorology/Inst. of Physics, University of Graz, Graz A-8010, Austria

Received 7 February 2013; received in revised form 14 May 2013; accepted 16 May 2013

Available online 23 May 2013

Abstract

Global Navigation Satellite System (GNSS) radio occultation (RO) is an innovative meteorological remote sensing technique for measuring atmospheric parameters such as refractivity, temperature, water vapour and pressure for the improvement of numerical weather prediction (NWP) and global climate monitoring (GCM). GNSS RO has many unique characteristics including global coverage, long-term stability of observations, as well as high accuracy and high vertical resolution of the derived atmospheric profiles. One of the main error sources in GNSS RO observations that significantly affect the accuracy of the derived atmospheric parameters in the stratosphere is the ionospheric error. In order to mitigate the effect of this error, the linear ionospheric correction approach for dual-frequency GNSS RO observations is commonly used. However, the residual ionospheric errors (RIEs) can be still significant, especially when large ionospheric disturbances occur and prevail such as during the periods of active space weather. In this study, the RIEs were investigated under different local time, propagation direction and solar activity conditions and their effects on RO bending angles are characterised using end-to-end simulations. A three-step simulation study was designed to investigate the characteristics of the RIEs through comparing the bending angles with and without the effects of the RIEs. This research forms an important step forward in improving the accuracy of the atmospheric profiles derived from the GNSS RO technique.

© 2013 COSPAR. Published by Elsevier Ltd. All rights reserved.

Keywords: Residual ionospheric errors; Bending angle; GNSS; Radio occultation

1. Introduction

GNSS RO, as a powerful and distinct atmospheric remote sensing technique used for monitoring the Earth's atmosphere physical properties such as refractivity, temperature, pressure and water vapour (Kursinski et al., 1997), is gradually becoming a significant data source for numerical weather prediction (NWP) (Kuo et al., 2000;

Le et al., 2010) and global climate monitoring (GCM) (Lackner et al., 2011; Steiner et al., 2011; Le et al., 2012). Both NWP and GCM play an important role in our daily lives and monitoring of weather/climate deterioration, to a certain extent caused by human activities. Evidence has shown that the average temperature of Earth's atmosphere rose significantly during the past century (Naidu et al., 2011), and global warming has increasingly threatened the Earth's ecological system. Therefore, the capability to observe the atmospheric temperature and identify its variation trend is significant for human beings. However, observing and forecasting the atmospheric temperature variation accurately and precisely remains a significant

* Corresponding author. Address: RMIT SPACE Research Centre, GPO Box 2476, Melbourne, Victoria 3001, Australia. Tel.: +61 451036606; fax: +61 3 96632517.

E-mail address: liucongliang1985@gmail.com (C.L. Liu).

challenge for meteorologists due to the extreme complexity and dynamic feature of the Earth's atmosphere and the limitations of current atmosphere observational instruments and techniques.

Radiosonde profiling has been the most dominant method for acquiring atmospheric profile information in the past seventy years and a global radiosonde network consisting of about 1900 stations has been developed worldwide so far (Kuo et al., 2005). GPS technology is regarded as an emerging space-borne technique for atmospheric observations, in particular the ground-based GPS technique that, for example, uses GPS continuously operating reference station (CORS) networks (Puviarasan et al., 2011). However, the spatio-temporal resolution of the radiosonde and ground-based GPS techniques are low due to the limitation of suitable geographic locations and high operational cost for global coverage.

Weather satellite remote sensing technology is also used for atmosphere observations and it has a high horizontal resolution and coverage but a low vertical resolution (Thies and Bendix, 2011). Almost all these techniques are prone to bias and drifting and complicated system calibration is usually required for global long-term climate observations (Gobiet and Kirchengast, 2004). Therefore, each of these techniques has its limitations when used for NWP and GCM. Fortunately, GNSS RO can solve many of these problems.

GNSS RO, realised so far as GPS RO, is an active satellite-to-satellite limb sounding technique (Melbourne et al., 1994; Kursinski et al., 1997; Hajj et al., 2002) where a dedicated GPS receiver aboard a LEO satellite is used to track L-band signals from GPS satellites. The overall effects on GPS signals due to the propagation path between GPS and LEO satellites (the atmosphere) lead to both propagation delay and refractive bending of the signals received. Fig. 1 shows the instantaneous GPS-LEO occultation geometry and its main parameters, in particular the bending angle as a function of impact parameter which is the focus variable of this study.

The RO principle was initially applied to planetary atmosphere and ionosphere detection, such as in the Mar-

iner 3 and 4 missions to Mars in the 1960s (Kliore et al., 1965; Fjeldbo and Eshleman, 1968). With the rapid development of GPS concept and system implementation in the 1970s, it became possible to observe the Earth's atmosphere using RO, and the concept was experimentally tested by the first experimental Global Positioning System/Meteorology (GPS/MET) mission launched in 1995 right after the full operational capacity of GPS was achieved. GPS/MET has demonstrated the unique properties of the GPS RO technique, such as high vertical resolution, high accuracy, all-weather capability and global coverage (Gorbunov et al., 1996; Ware et al., 1996; Rocken et al., 1997; Steiner et al., 1999). It was proved that RO data have a great potential to play a significant role in atmospheric process studies, NWP and GCM applications.

The subsequent LEO satellite missions such as the CHALLENGING Minisatellite Payload (CHAMP), the Constellation Observing System for Meteorology, Ionosphere and Climate (COSMIC), the Gravity Recovery And Climate Experiment (GRACE), and the Meteorological Operational (MetOp) satellites have further affirmed the long-term stability and remarkable consistency (e.g., <0.2 – 0.5 K in temperature) of RO observations from different RO missions (Foelsche et al., 2009, 2011). With the advanced development of inversion and assimilation algorithms, GPS RO has been widely used to enhance NWP and GCM in many weather institutes since a great amount of globally-distributed high-quality GPS RO data has been accumulated at main RO data processing centre that can be used to analyse weather and climate of the past decades.

Recent rapid development in GNSS, such as the Russia's GLONASS, China's Beidou and the European Galileo systems, has significantly enhanced the availability and capacity of the GPS-like satellites which will make RO even more attractive in the future. These new generation GNSS, coupled with planned LEO missions will offer many new transmitter platforms for RO observations. It is believed that the robust GNSS RO method has a great potential to deliver climate benchmark measurements (Steiner et al., 2011), due to its unique characteristics aforementioned, that are traceable to the international time standard (e.g. self-calibration through differencing method and dual-frequency ionospheric correction).

However, GNSS RO is affected by a variety of (small) uncertainties or errors, such as the orbital errors, clock bias, systematic hardware signal delays, antenna phase center variation, cycle slips, observation noise, ionosphere refraction, atmospheric multipath, relativistic effects (Kursinski et al., 1997; Scherllin-Pirscher et al., 2011). Several studies show that these errors and biases can be mitigated effectively to obtain high accuracy atmospheric parameter profiles at altitudes of about 10–35 km, but the errors increase significantly above 35 km, especially at the altitudes above 50 km (Kursinski et al., 1997; Rieder and Kirchengast, 2001; Gobiet and Kirchengast, 2004). The main problem is that the signal-to-noise ratio of GNSS RO observations decreases with the increase of the height

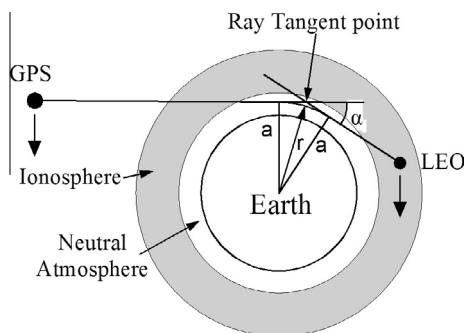


Fig. 1. Radio occultation geometry (α is the bending angle, a is the impact parameter, which is the perpendicular distance between the ray asymptotes and the centre of refraction, r is the radius of GPS-LEO signal path curvature).

towards the stratopause and into the mesosphere where the thermal noise and the residual ionospheric errors (RIEs) become increasingly dominant (Rieder and Kirchengast, 2001; Steiner and Kirchengast, 2005). This suggests that one of the challenging areas in GNSS RO retrieval lies in the upper stratosphere and mesosphere.

RIEs refer to the residual ionospheric errors after an ionospheric correction by linear combination of dual-frequency GNSS RO observations is applied. RIEs are regarded as the most dominant error in RO bending angle retrievals at high altitudes, due to the dynamic and complex nature of the ionosphere structure. Usually, RIEs and other high-altitude errors are further mitigated by applying a statistical optimization method, which uses a suitable background bending angle profile to enable improved retrievals (Syndergaard, 2000; Healy, 2001; Gobiet and Kirchengast, 2004).

Traditionally, dual-frequency linear ionospheric corrections for two types of data—excess phases and bending angles—are used to mitigate the ionospheric errors. Studies (Vorobev and Krasilnikova, 1994; Steiner et al., 1999; Gobiet and Kirchengast, 2004) in RO data processing have shown that the ionosphere combination of bending angles performs better than that of excess phases. Hence, the RIEs of bending angles at above 50 km altitude are the focus of this simulation study.

In Section 2, RIEs will be first elaborated, followed by a brief introduction of the related methodologies including ray tracing in Section 3, simulation design and results analysis in Section 4. A summary, main conclusions and an outlook of this study will be given in Section 5.

2. Residual ionospheric errors

The physical properties of the neutral atmosphere such as refractivity, temperature, pressure and density retrieved from bending angles are essential for NWP and GCM. However, the signal's bending is originated from both the neutral atmosphere and the ionosphere and the atmospheric parameters to be used for NWP and GCM must be based on the effects of the neutral atmosphere only. Thus, it is necessary to eliminate the ionospheric effects for meteorological applications.

2.1. Ionospheric effects on wave propagation

The Earth's ionosphere is the upper atmospheric region, located at the altitude range of around 60–1500 km where a large number of ionised molecules and free electrons exist that affects electromagnetic wave propagation. Eqs. (1) and (2) below are the Appleton–Hartree formula and its series expansion (Bissiri and Hajj, 1993; Ladreiter and Kirchengast, 1996; Norman et al., 2013), respectively, for the phase refractive index (n) in the ionosphere:

$$n^2 = 1 - X(U - X) / \left[U(U - X) - 0.5Y^2 \sin^2 \theta \pm \sqrt{0.25Y^4 \sin^4 \theta + Y^2 \cos^2 \theta (U - X)^2} \right] \quad (1)$$

$$n \approx 1 - 0.5X \pm 0.5XY |\cos \theta| - 0.125X^2 - 0.25XY^2 (1 + \cos^2 \theta) - 0.5iXZ \quad (2)$$

$$X = \omega_p^2 / \omega^2, \quad Y = \omega_c / \omega, \quad Z = \vartheta_e / \omega, \quad U = 1 - iZ, \\ \omega_p^2 = e^2 N_e / (m \epsilon_0), \quad \omega_c = eB / m, \quad \text{and } \vartheta_e \propto \exp(z/H).$$

where

ω_p is the electron angular plasma frequency,
 ω_c is the electron gyro-frequency,
 ω is the propagating wave angular frequency,
 θ is the angle between magnetic field and the wave normal,
 ϑ_e is the electron collision frequency,
 e is the elementary charge,
 N_e is the electron density,
 m is the electron mass,
 ϵ_0 is the permittivity of vacuum,
 B is the ambient geomagnetic field strength,
 z is the altitude, and
 H is the scale height.

At the GPS signal frequencies of L1 and L2 ($f_1 = 1.57542$ GHz and $f_2 = 1.22760$ GHz), the order of magnitudes of the five terms in Eq. (2) is: 1, 10^{-4} , 10^{-7} , 10^{-9} , 10^{-10} and $i10^{-9}$, respectively. In GNSS RO data processing for neutral atmosphere sounding, the last four terms can be neglected, of which the geomagnetic term with its 10^{-7} order of magnitude is the relatively most important higher-order term (Ladreiter and Kirchengast, 1996; Syndergaard, 2000; Hoque and Jakowski, 2010). We performed test simulations, similar to those discussed in Section 4, where we both included and excluded this geomagnetic term of 2nd order and found it to have no appreciable effect on the bending angle RIEs. As a result, the ionospheric refractive index of GPS signals can be expressed for the present purpose as:

$$n \approx 1 - C \cdot N_e / f_i^2, \quad (3)$$

where $C = e^2 / (8\pi^2 m \epsilon_0)$ is a constant, and $i = 1, 2$ corresponds to the L1 and L2 signal frequencies, respectively. According to Eq. (3), electron density N_e is the key physical quantity of the ionosphere in RO data processing due to its dominant effect on electromagnetic wave propagation.

For GPS L band signals, the refractive index effect of free electrons is larger than that of the neutral gas per unit mass. The maximum day time ionosphere refractive index effect is at a height of around 300 km, where the combination of abundant extreme ultraviolet solar radiation intensity and sufficient atmospheric density causes an ionisation

maximum. It is comparable to the atmosphere refractive index at a height of around 30 km. Hence an ionospheric correction is necessary for high accuracy atmospheric parameter retrievals, especially for climate benchmark applications. The most common approach to initially correcting the ionospheric effect is to use a linear combination of GPS dual-frequency observations in the GNSS RO technique, which is discussed in Section 2.2.

2.2. Dual-frequency observation combinations

The ionosphere is a dispersive medium for L band signals, i.e., the ionospheric refractive index of the GNSS signals are approximately proportional to the inverse of the square of the signal frequency ($1/f^2$), this can be seen from the second term on the right-hand side of Eq. (3). In contrast, the frequency dispersion of the neutral atmosphere is negligible at L band signals. Therefore, a linear combination of the phases or bending angles of L1 and L2 signals can be used to eliminate most of the ionospheric effects on them. Commonly, a classical linear combination of L1 and L2 phase observations or the linear combination of their corresponding bending angles are used in GNSS RO to mitigate the ionospheric errors (Gobiet and Kirchengast, 2004), as expressed by Eqs. (4) and (5), respectively.

$$L_c(t) = (f_1^2 L_1(t) - f_2^2 L_2(t)) / (f_1^2 - f_2^2), \quad (4)$$

where $L_c(t)$ is the ionosphere-corrected phase from linear combination of L1 and L2, t is the observation time, $L_1(t)$ and $L_2(t)$ are the phase observations of the signals on L1 and L2, respectively, at time t .

$$\alpha_c(a) = (f_1^2 \alpha_1(a) - f_2^2 \alpha_2(a)) / (f_1^2 - f_2^2), \quad (5)$$

where $\alpha_1(a)$ and $\alpha_2(a)$ are the bending angles derived from the L1 and L2 signals at the impact parameter a , and $\alpha_c(a)$ is the resulting ionosphere-corrected bending angle from dual-frequency linear combination of $\alpha_1(a)$ and $\alpha_2(a)$.

The dual-frequency ionospheric correction of phases has been widely used in navigation and positioning applications, and was also used in the first stage of GNSS RO data processing. It is based on the assumption that the L1 and L2 signals share the same ray path when they pass through the ionosphere and neutral atmosphere. In fact, the two signals follow different ray paths due to the dispersion of the ionosphere, and the separation of the two paths is substantial in RO measurement, which results in relatively large phase RIEs. Vorobev and Krasilnikova (1994) introduced a dual-frequency ionospheric correction of bending angles at the same impact parameter a , as expressed by Eq. (5). Several theoretical (Vorobev and Krasilnikova, 1994) and simulation studies (Gobiet and Kirchengast, 2004; Fritzer et al., 2011) showed that this combination provides better results than that of the phase combination by Eq. (4) since it not only accounts for the different ray paths of the dual-frequency signals but also considers the fact that most of the

total bending angle is accumulated near the ray perigee (Ladreitner and Kirchengast, 1996). The two ray paths at the same impact parameter are closer than those at the same time, but they are still slightly different paths.

In the RO technique, the RIEs after performing those linear ionospheric corrections are mainly caused by the separation of the L1 and L2 signal ray paths when passing through the atmosphere. Another source of the RIEs are, in principle, higher-order terms of the ionospheric refractive index, which are not proportional to the inverse square of the signal frequency ($1/f^2$) and affected by the geomagnetic field. As discussed above these higher-order terms can be disregarded in the analysis, however, since the effects from the first order term strongly dominate in the RIEs.

The RIEs of bending angle will affect the accuracy of atmospheric profile retrievals. For high accuracy meteorology monitoring and benchmark climate applications, more effective algorithms or approaches for mitigating the effects of the RIEs are needed. In this study, a simulation of high-altitude bending angle RIEs using the ray tracing technique was conducted to investigate the characteristics of the bending angle RIEs in various ionospheric conditions, in which the NeUoG (electron density university of Graz) ionosphere model (Leitinger et al., 1996) and the MSIS90 neutral atmosphere model (Hedin, 1991) were used as the atmospheric models.

3. Methodology

3.1. Ray tracing method

The ray tracing technique is commonly used for calculating the path of an electromagnetic signal in a medium specified by a position-dependent refractive index, such as the Earth's atmosphere. It has become a significant tool to investigate GPS signal's propagation. Particularly, it has been used in GNSS RO technology to study how the ionosphere affects the accuracy of the neutral atmospheric parameter retrievals. It has been also used to validate how the signals' separation contributes to the excess phase RIEs (Syndergaard, 2000). Furthermore, Hoque and Jakowski (2010) used this method to study the effects of higher order ionospheric terms on the propagation of GPS RO signals through the ionosphere. They found raypath separations of L1 and L2 of up to about 1 km and higher-order effects to be comparatively small. Mannucci et al. (2011) used ray tracing to analyse the magnitude of bending angle RIEs under ionospheric storm conditions by studying the propagation of GPS signals in RO geometry. They concluded that RO retrievals above about 25–30 km could be significantly degraded from ionospheric storm effects.

In this study, a 3-D numerical ray tracing technique was used to simulate the GPS signals received by LEO satellites to obtain excess phases, subsequently leading to retrieved bending angle profiles, as part of an end-to-end RO simulation tool (Fritzer et al., 2011), and utilising it for various ionospheric conditions.

3.2. Atmospheric and ionospheric modelling

The focus of this study is to investigate the characteristics of the RIEs in various ionospheric conditions rather than the errors caused by the neutral atmosphere. The MSIS-90 (Hedin, 1991) neutral atmospheric model was adopted in the forward modelling process, since it is a simple yet representative atmospheric reference model. Furthermore, in order to derive reliable bending angle RIEs using the dual-frequency linear combination without any gradient effects of the neutral atmosphere, a dry atmosphere and local spherical symmetry atmosphere mode was used during the simulations. In this case, the neutral atmospheric refractivity depends essentially on the atmospheric pressure P and temperature T . Eq. (6) represents the dry neutral atmospheric refractivity:

$$N = 77.6P/T. \quad (6)$$

Regarding the ionosphere, the NeUoG ionospheric model was used in this study (Ladreiter and Kirchengast, 1996; Leitinger and Kirchengast, 1997). This model represents the 3D electron density distribution as a function of local time, season, and solar activity. It well represents realistic large-scale ionospheric variability but does not include small-scale ionospheric structures. Ionospheric refractivity can be obtained from the NeUoG by the approximated Appleton–Hartree formula according to Eq. (3). Therefore, the simulated RIEs in this study do not consider the effects of small-scale ionospheric structures and of higher-order ionospheric refraction terms (which were found not relevant for the present purpose as discussed in Section 2.1).

3.3. Simulation of a RO event

Fig. 2 sketches the simulation process for the RO events. The relevant raw RO observations are the excess phase time series of GPS signals, simulated by forward modelling, based on which Doppler shifts can be obtained by time derivation of the excess phase time series as a first step of bending angle retrieval. Bending angle profiles as a function of impact parameter can then be derived using both the Doppler shift time series and precise orbit arc data of the GPS and LEO satellites (i.e., positions and velocities). The ionospheric effects on the L1 and L2 raw bending angles can be corrected for by the dual-frequency linear combination of the bending angles discussed in Section 2.2 above.

In summary, as illustrated in Fig. 2, the whole process of simulating a single RO event towards ionosphere-corrected bending angles consists of the following five stages: (1) satellite geometry simulation, (2) modelling of the neutral atmosphere and ionosphere, (3) simulation of GNSS dual-frequency signals' propagation through the atmosphere, (4) simulation of the observation system and its influences on the signals (like attenuation due to geometrical dilution, i.e., space loss, or receiver thermal noise), and (5) retrieval of bending angles and ionospheric correction.

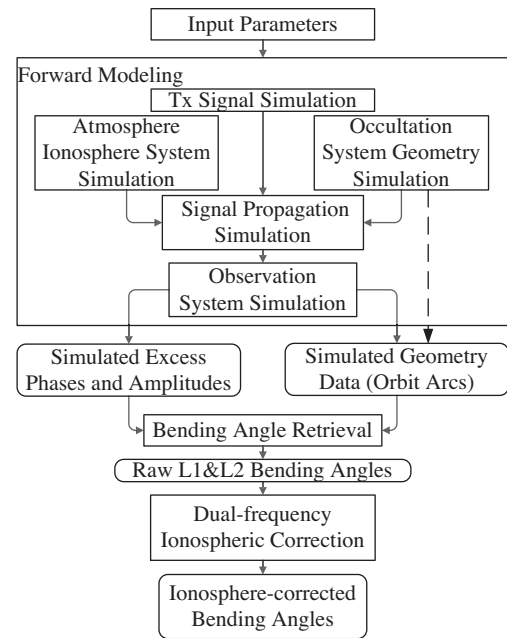


Fig. 2. Flow chart of the RO end-to-end simulation process for bending angles.

We note that we did not superpose any observation system error sources such as receiver thermal noise or clock noise in the simulations for this study in order to focus on estimating the RIEs without additional error sources. The End-to-end Generic Occultation Performance Simulation and Processing System (EGOPS) (Fritzer et al., 2011) has all these process steps implemented—see, e.g. Steiner and Kirchengast (2005) as an instructive end-to-end application example—and was used to carry out this study.

4. RIEs study procedure and preliminary results

4.1. Simulation design

The following three steps were designed to generate the RIEs. (1) Bending angles that do not contain ionospheric error effects are simulated first and these bending angles are used as ‘no-error’ reference bending angles for subsequent research. (2) Bending angles for both GPS frequencies that contain ionospheric effects are then simulated and a dual-frequency ionosphere-corrected bending angle is computed (so that the resulting neutral atmosphere bending angle contains RIEs). (3) Finally, the RIEs themselves are estimated by differencing the bending angles with and without the effects of the ionosphere.

In this study, 14 different RO events were simulated with EGOPS (Fritzer et al., 2011), which represents a variety of combinations of two different local times, two different directions of RO planes and three intensity levels of solar activities. All the 14 events were at 12:00 UTC (coordinated universal time) on 15 July, 2008, and two of these 14 events were simulated without ionosphere and used as reference events that are free of ionosphere effects.

Two geographical locations ([40°N, 75°W] and [40°N, 45°E]) corresponding to the two local times of 7:00 and 15:00, respectively (see the two red triangles in Fig. 3 discussed below), were utilised to construct the other 12 RO events. The two directions of the RO occultation planes selected were formed by setting the azimuth angles to 0° and 90°, respectively, and the three ionisation levels (low, medium and high solar intensities) were obtained by setting F10.7 indices to 70, 140 and 210, respectively. The simulation characteristics of the 12 RO events are summarized in Table 1.

Fig. 3 illustrates the global distribution of vertical total electron content (VTEC) as a function of latitude and longitude at 12:00 UTC on 15 July, 2008 calculated by using NeUoG under the aforementioned three ionisation levels. Table 2 presents the global maximum VTEC and the VTECs at the two RO event locations (Locations 1 and 2) for each subpanel in Fig. 3. From Table 2 and Fig. 3 it can be seen that the VTEC values at the three ionisation levels are ranging up to about 26, 52, and 90 total electron

content (TEC) units (one TECU = 10^{16} electrons/m²), respectively. Comparing the VTEC values of the two locations at the same solar intensity level (i.e., in the same subpanels of Fig. 3), we can see that the differences can reach about 4, 10 and 18 TECUs, respectively.

Fig. 4 depicts longitude-height cross sections of electron density and three representative ray paths of each RO event in the longitudinal direction. Table 3 lists TEC along the ‘inbound’ and ‘outbound’ segments of each ray path in Fig. 4. As demonstrated in the three subpanels of Fig. 4 and in Table 3, TEC and electron density gradients along the ray paths increase significantly with the increase of the F10.7 values. For example, the TEC along the lowermost ray path above Location 1, Inbound plus Outbound, increases from about 10 TEC units when F10.7 is 70, to about 20 TEC units when F10.7 is 140, then to about 35 TEC units when F10.7 is 210. These values above Location 2 are from about 20–39 TEC units then to 67 TEC units. Comparing the electron density values around the ray paths at the two locations for each subpanel, one can see that the

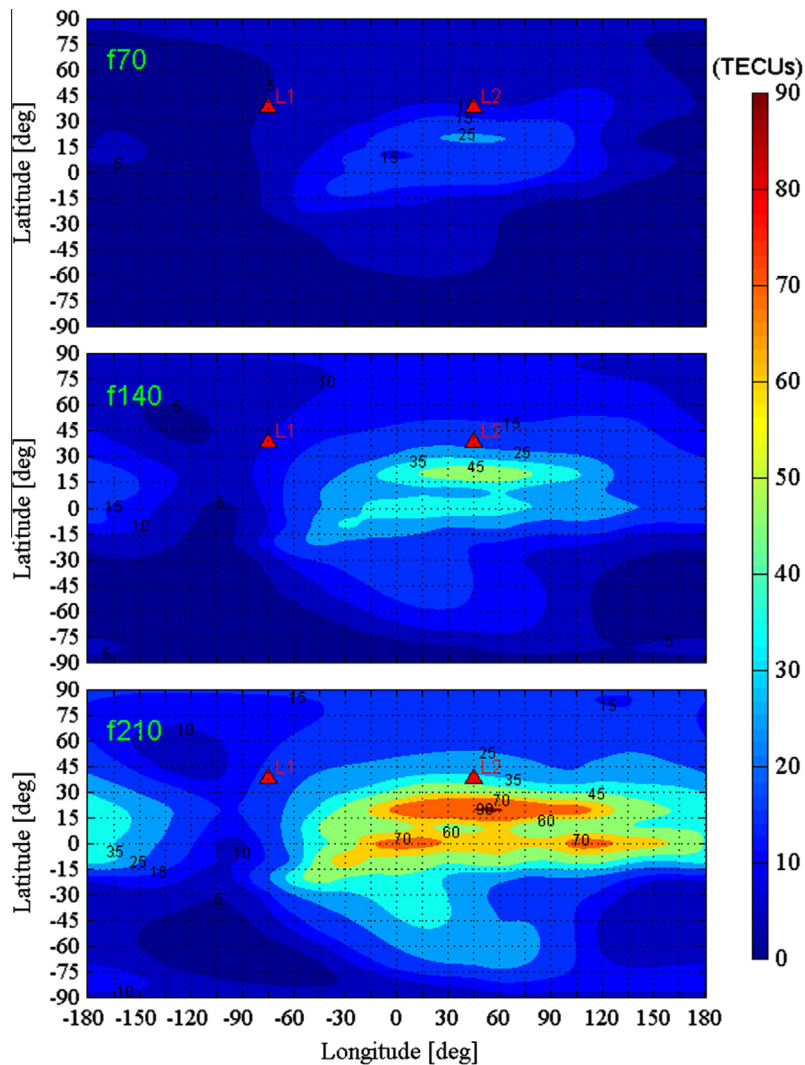


Fig. 3. Distributions of VTEC in TEC units ($1 \text{ TECU} = 10^{16} \text{ m}^{-2}$) for three ionisation levels ((f70) F10.7 = 70, (f140) F10.7 = 140, (f210) F10.7 = 210) and two RO locations: Location-1 (40°N, 75°W, L1) and Location-2 (40°N, 45°E, L2).

Table 1
The characteristics of the 12 simulated RO events.

RO event	Location	Local time	RO plane azimuth	RO plane direction	F10.7 index
<i>Longitudinal RO events in Fig. 4 and Table 3</i>					
17a90f70	40°N 75°W	7: 00	90°	East–West	70
17a90f140	40°N 75°W	7: 00	90°	East–West	140
17a90f210	40°N 75°W	7: 00	90°	East–West	210
115a90f70	40°N 45°E	15: 00	90°	East–West	70
115a90f140	40°N 45°E	15: 00	90°	East–West	140
115a90f210	40°N 45°E	15: 00	90°	East–West	210
<i>Latitudinal RO events in Fig. 5 and Table 4</i>					
17a0f70	40°N 75°W	7: 00	0°	South–North	70
17a0f140	40°N 75°W	7: 00	0°	South–North	140
17a0f210	40°N 75°W	7: 00	0°	South–North	210
115a0f70	40°N 45°E	15: 00	0°	South–North	70
115a0f140	40°N 45°E	15: 00	0°	South–North	140
115a0f210	40°N 45°E	15: 00	0°	South–North	210

Table 2
Global maximum VTEC values and the VTECs of Location-1 and Location-2 (in TEC Units).

F10.7	Global maximum VTEC	VTEC (Location-1)	VTEC (Location-2)
70	26.27	5.17	9.48
140	51.67	9.90	19.95
210	90.35	17.03	35.20

electron density gradients vary more drastically above Location 2 than Location 1. On the other hand, the TECs along the Inbound and Outbound segments of the ray paths at Location 2 are relatively symmetrical, which are different from the asymmetrical feature of the ray paths at Location 1. The values of the differences between the Inbound and the Outbound TECs, i.e., the ‘Difference’ column of Location 1 in Table 3, also indicate this feature.

Similarly, Fig. 5 shows latitude-height cross sections of the electron density of the other six RO events with azimuth along the latitudinal direction. Fig. 5 contains six subpanels, rather than three as in Fig. 4, because the two RO event locations are at different longitudes. Table 4 lists the TEC along the ‘inbound’ and ‘outbound’ segments of each ray path in Fig. 5. It can be seen that, at different solar activity levels and at different RO locations, the ionospheric conditions of these RO events are significantly different. The features of the electron density distribution such as gradients and symmetry are similar to the longitudinal-direction events shown in Fig. 4. Comparing Fig. 5 (Table 4) with Fig. 4 (Table 3), we can find that the latitudinal RO events are affected by the equatorial anomaly more than the longitudinal events, however, especially for the RO events at Location 2. Comparing the differences between TECs of the Inbound and Outbound segments of the ray paths above Location 2 in Table 3 to that in Table 4, we can also find that the difference values of the latitudinal ray paths are 12–36 TEC units larger than those of the longitudinal ray paths, reflecting the strong influence of the equatorial anomaly features.

4.2. Simulation results for ionospheric and atmospheric bending angles

The simulated bending angles and the reference bending angles are compared in Figs. 6 and 7. The title in each of the panels contains parameter information of local time, the azimuth of the RO plane (relative to the North direction, counter-clockwise) and the solar intensity level, e.g. “17a0f70” means the RO event’s local time of 7:00, the azimuth of the RO plane of 0° (i.e., south-to-north) and the solar activity intensity of 70. In these panels, the MS (mesosphere), the US (upper stratosphere) and the LS (lower stratosphere) correspond to the impact heights in the ranges of 50–80 km, 35–50 km and 15–35 km, respectively; α_1 , α_2 , α_c and α_{ref} denote the bending angles of L1 and L2, ionosphere-corrected and the reference bending angles (with no ionosphere), respectively. In Figs. 6 and 7, the upper panels are for the results over the whole profile of the bending angles (in units mrad), and the middle and bottom panels are enlarged graphs for the two impact height ranges of core interest (in units μ rad), for a detailed comparison of α_1 , α_2 , α_c and α_{ref} in the MS and US layers. Of the 12 events investigated, only the results of three morning latitudinal-direction events are shown in Fig. 6, and three afternoon longitudinal direction events in Fig. 7, since all the other events show similar features.

From Figs. 6 and 7, comparing the three subpanels in each row that correspond to the same height range but different ionisation levels, one can find that the differences between α_1 and α_2 at the same height increase with the rise of the solar intensity level; at the level of F10.7 = 210, the maximum differences between α_1 and α_2 in the MS (see 115a90f210-MS) and US (L15a90f210-US) can reach about 70 μ rad (at the height of 80 km) and about 50 μ rad (at the height of 50 km), respectively. This suggests both the mesosphere and the upper stratosphere are significantly affected by the ionospheric effects. Figs. 6 and 7 also show that both α_c and α_{ref} curves are close. This suggests that the dual-frequency linear combination of bending angles (Eq. (5)) can mitigate most of the ionospheric effects. However, the

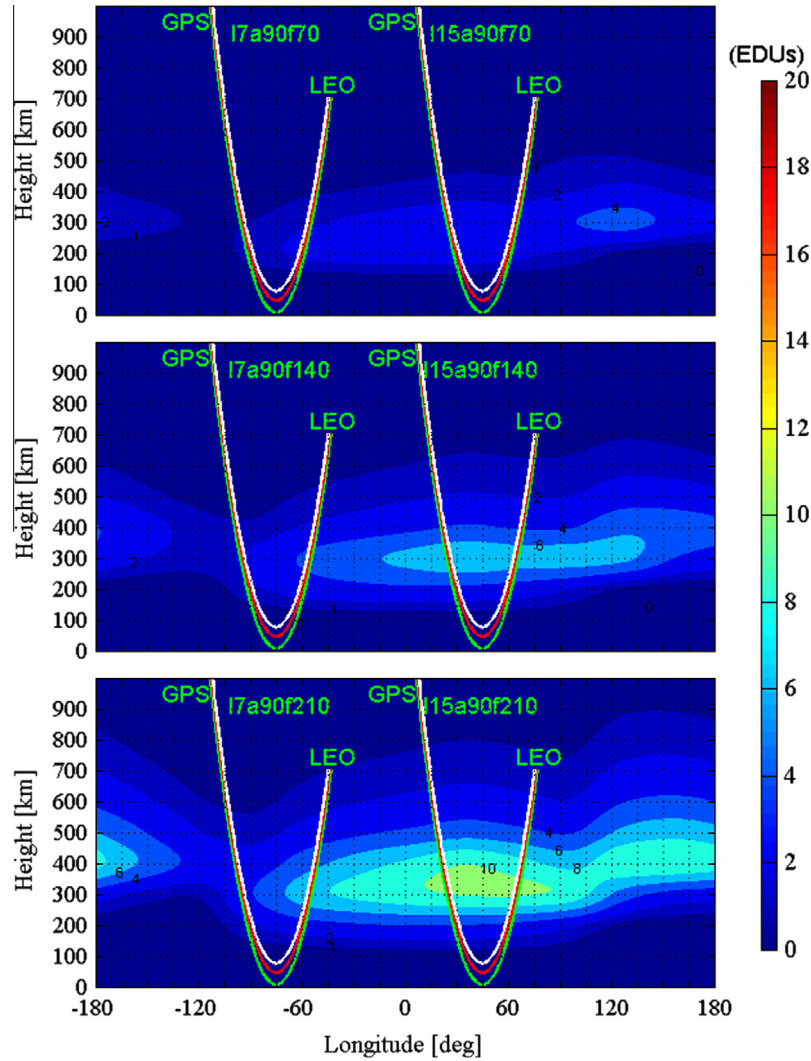


Fig. 4. Height-vs-longitude cross-sectional views of electron density in electron density units ($1 \text{ EDU} = 10^{11} \text{ m}^{-3}$) at 40°N at three ionisation levels ($f70$) $F10.7 = 70$, ($f140$) $F10.7 = 140$, ($f210$) $F10.7 = 210$) and the lowermost ray path (green), stratopause ray path (red) and mesopause ray path (white) of the longitudinal-direction RO events, which are corresponding to the heights of tangent points at 10, 50 and 80 km, respectively. (For interpretation of the references to color in this figure legend, the reader is referred to the web version of this article.)

Table 3

TEC values along the inbound and outbound of the ray paths (longitudinal) (in TEC Units).

F10.7	TP height [km]	TEC (Location-1)			TEC (Location-2)		
		Inbound	Outbound	Difference	Inbound	Outbound	Difference
70	10	3.12	6.80	-3.68	10.12	9.65	0.47
	50	3.27	6.74	-3.47	10.13	9.56	0.57
	80	3.35	6.68	-3.33	10.13	9.51	0.62
140	10	6.19	13.65	-7.46	20.54	18.52	2.02
	50	6.44	13.52	-7.08	20.57	18.61	1.96
	80	6.57	13.39	-6.82	20.60	18.65	1.95
210	10	10.74	23.95	-13.21	35.71	31.12	4.59
	50	11.13	23.71	-12.58	35.77	31.51	4.26
	80	11.33	23.46	-12.13	35.83	31.71	4.12

wave-like curve of the α_c profile, especially under high solar activity environments, e.g., in the cases of $F10.7 = 210$ and the afternoon events, indicates that α_c contains RIEs. As discussed in Section 1, for the RO results the RIEs can

be the main error source in the mesosphere and the upper stratosphere regions, particularly at high ionisation levels. In Section 4.3, the absolute RIEs and relative RIEs will be investigated and analysed.

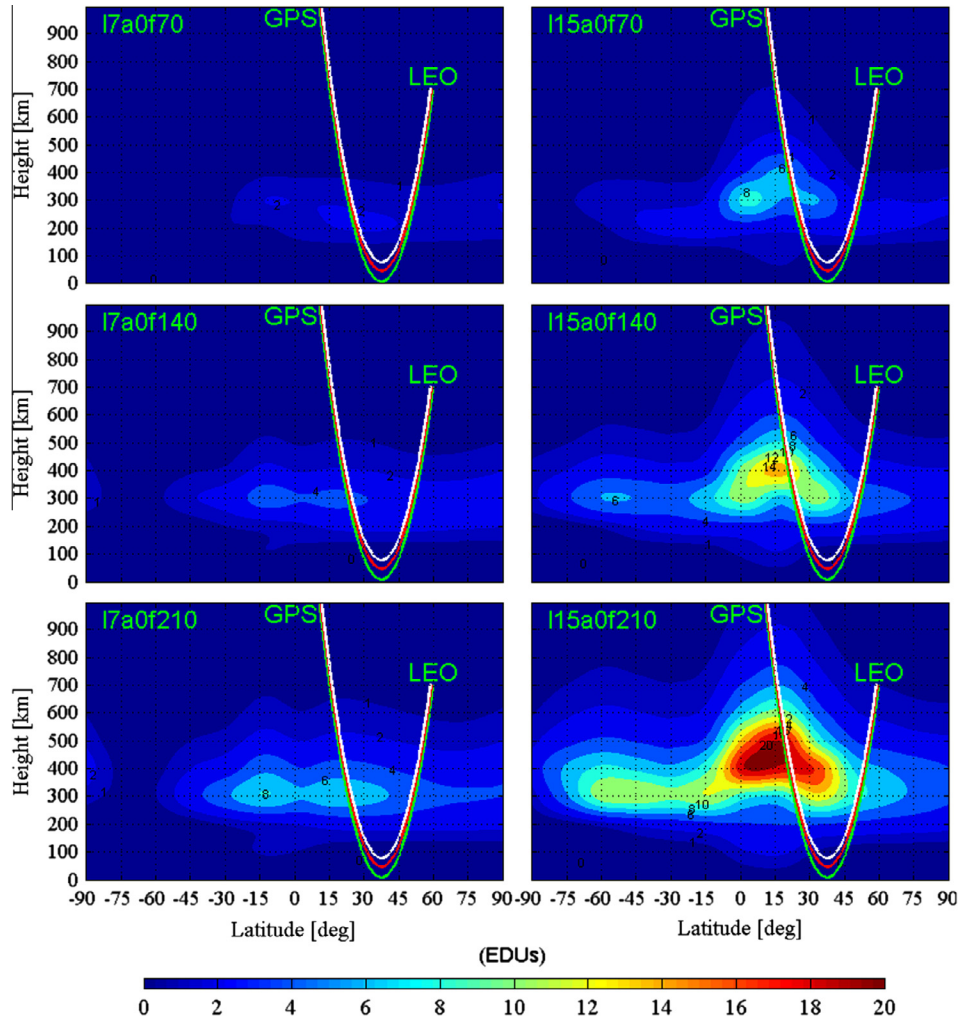


Fig. 5. Height-vs-latitude cross-sectional views of electron density in electron density units ($1 \text{ EDU} = 10^{11} \text{ m}^{-3}$) at 75°W (left panels) and 45°E (right panels) for three ionisation levels ((f70) $F10.7 = 70$, (f140) $F10.7 = 140$, (f210) $F10.7 = 210$) and ray paths of the latitudinal-direction RO events (the lowest ray path (green), stratopause ray path (red), mesopause ray path (white)), which are corresponding to the heights of tangent points at 10, 50, and 80 km, respectively). (For interpretation of the references to color in this figure legend, the reader is referred to the web version of this article.)

Table 4
TEC values along the inbound and outbound of the ray paths (latitudinal) (in TEC Units).

F10.7	TP height [km]	TEC (Location-1)			TEC (Location-2)		
		Inbound	Outbound	Difference	Inbound	Outbound	Difference
70	10	6.32	4.89	1.44	24.29	7.07	17.21
	50	6.26	4.88	1.38	23.29	7.13	16.17
	80	6.20	4.88	1.31	22.30	7.18	15.13
140	10	12.04	8.55	3.50	47.88	13.63	34.24
	50	11.95	8.58	3.37	45.98	13.85	32.13
	80	11.86	8.61	3.25	44.08	14.06	30.02
210	10	20.22	13.94	6.28	83.25	23.76	59.49
	50	20.08	14.08	6.00	79.95	24.18	55.78
	80	19.93	14.22	5.72	76.66	24.59	52.07

4.3. Simulation results for RIEs

Figs. 8 and 9 show the absolute and relative RIEs profiles of the simulated bending angles and indicate statistical results (bias, standard deviation) over four atmospheric layers, from lower stratosphere to upper mesosphere. Fig. 10 provides a summary illustration of the bias and

standard deviation results. The absolute RIEs are the difference between the α_c and α_{ref} profiles. The relative RIEs are obtained from the absolute RIEs divided by α_{ref} and multiplied by 100 (to be in units [%]). For both the absolute and relative RIE profiles, the standard deviation, the bias (layer average of the RIEs) and the 95%-confidence range of the bias (i.e., the 2σ standard uncertainty of the

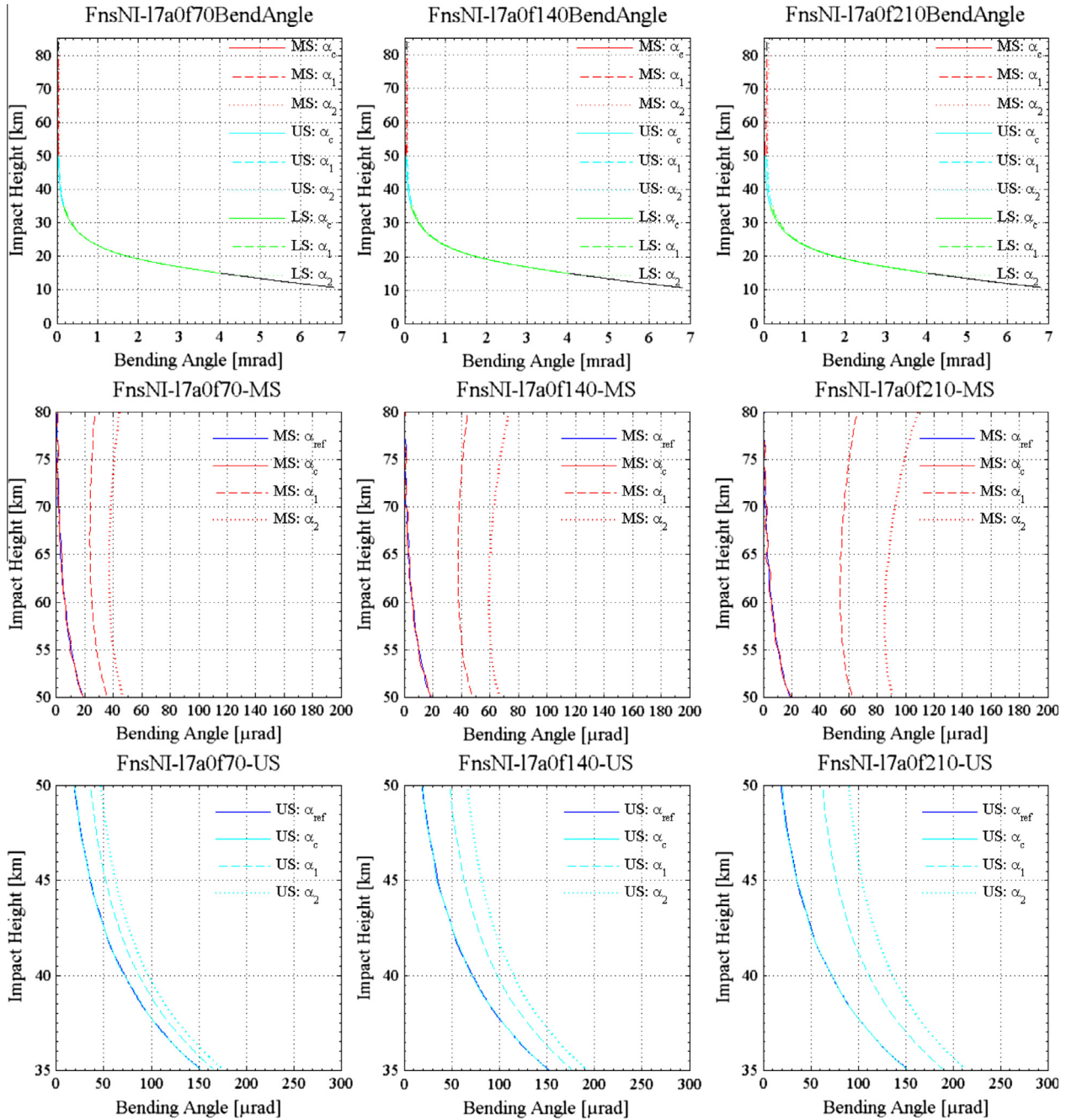


Fig. 6. Bending angle simulation results for the three morning latitudinal events and comparisons with their reference bending angles in the MS and US regions. Each panel row shows the bending angles at all the three ionisation levels (70, 140, 210).

layer-averaged RIEs) were calculated for each of the four atmospheric layers. They are shown as values in the in-panel legends.

We note that the simulations for this study were done at a 10 Hz sampling rate for the data. Preliminary results for a 50 Hz sampling rate – the sampling rate typically used by real RO receivers – show somewhat smaller but similar RIEs. The detailed magnitudes depend on forward modeling details and also on the noise filtering applied in the retrieval of the bending angle from the excess phase profiles.

From Fig. 8 we can see that in the LM layer the maximum absolute RIE reaches 2.1 μ rad and the minimum

RIE is -1.8μ rad; and in the US layer these values are 2.0 and -1.6μ rad, respectively. All the 12 panels show that the standard deviations are in the range of 0.3–1 μ rad and 0.3–0.7 μ rad in the LM and the US regions, respectively. From the six morning events (see the top six panels), the maximum RIE bias magnitudes are 0.059 and 0.036 μ rad in the LM and US layers, respectively; and these values in the afternoon events (the bottom six panels) are 0.091 and 0.068 μ rad. In terms of sign, the small RIE biases have a clear tendency to be negative, which is in line with estimations in other studies that also used real RO data (Danzer et al., 2013). Although the values of the RIEs are small,

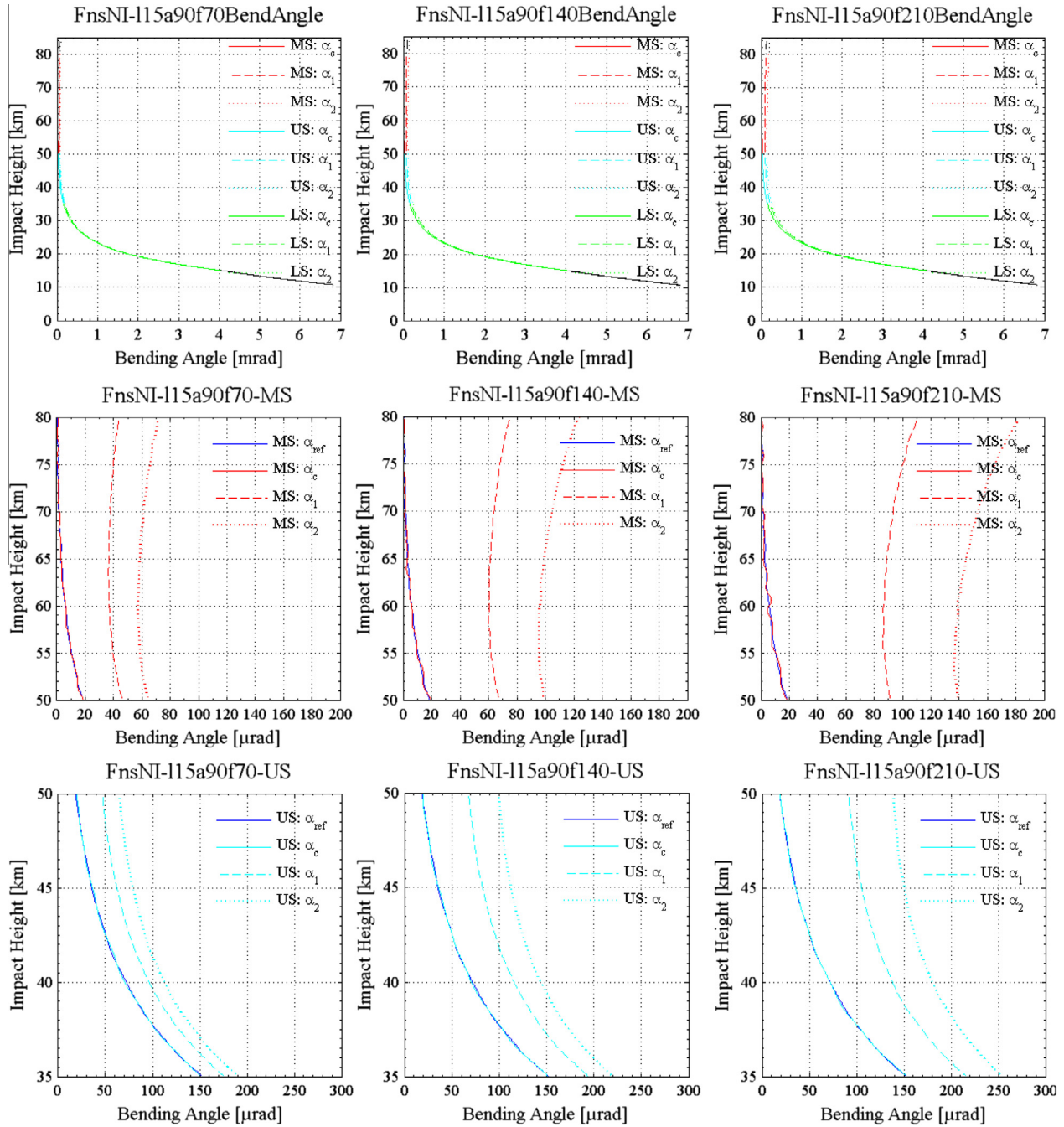


Fig. 7. Bending angle simulation results for the three afternoon longitudinal events and comparisons with their reference bending angles (the layout is the same as for Fig. 6).

they can still be the dominant residual errors in the LM and US regions, where the values of the bending angles are also small due to the low density of the neutral atmosphere.

Fig. 9 shows the relative RIEs profiles of the bending angles in all the four atmospheric layers, including our main research interest regions of UM, LM and US. Based on the 12 cases, the following conclusion can be drawn: (1) at the impact heights above 65 km, i.e., the upper mesosphere (UM), most relative RIE standard deviations reach about 50% or more; (2) in the 50–65 km impact height

range, i.e., the lower mesosphere (LM), relative RIE standard deviations still reach about 5–15%; and (3) in the US, the relative RIE standard deviations amount to roughly around 1%. As expected based on Fig. 8, relative RIEs generally increase with increasing ionisation levels.

Fig. 10 shows, as a summary, the values and the solar activity dependence of the absolute bending angle RIE biases and standard deviations in LM, US, and the full 30–80 km impact height region, respectively, for the 12 RO events. The RIE magnitudes of typically 0.3–0.7 μrad,

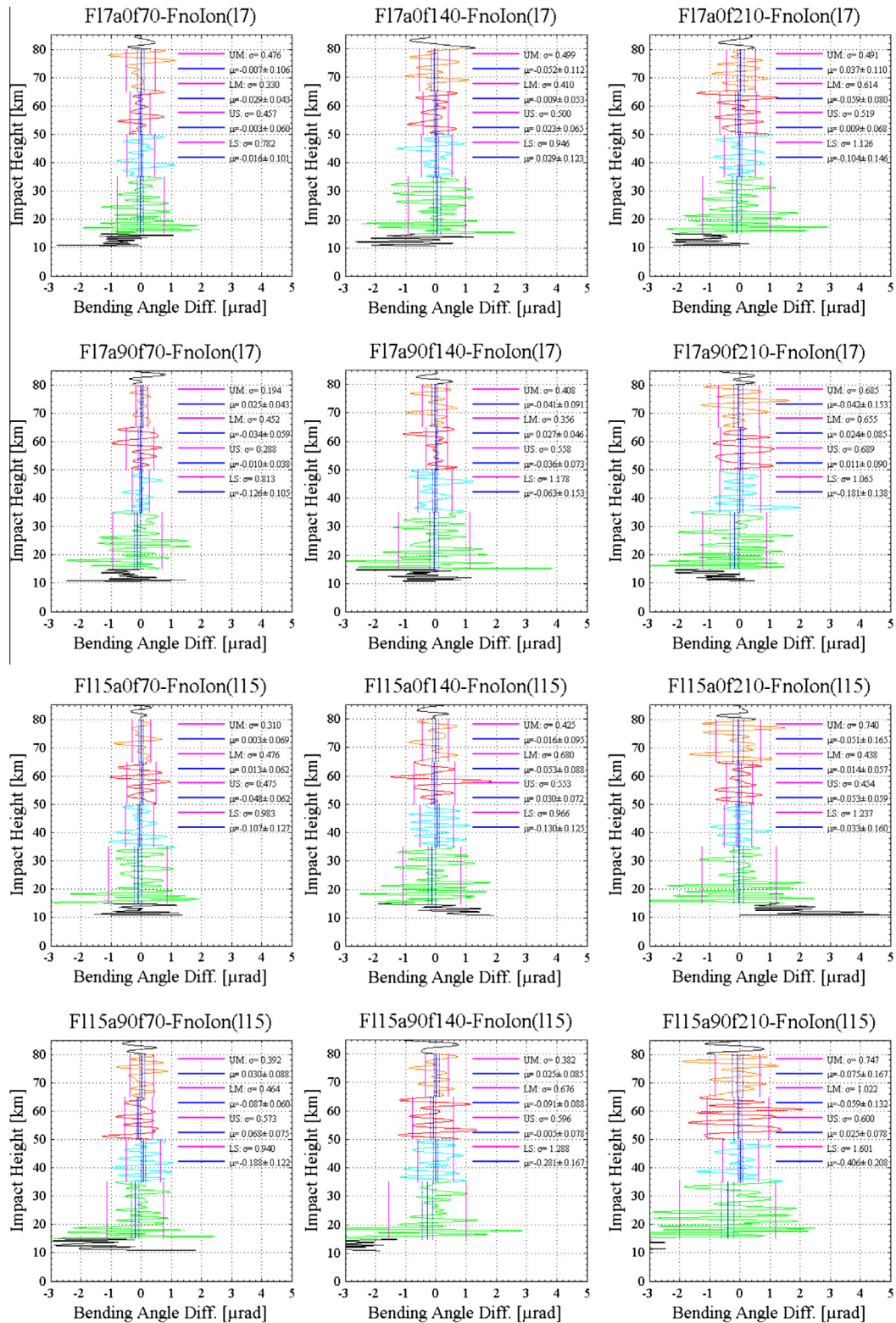


Fig. 8. Absolute RIE profiles of the simulated bending angles and their statistical results over four characteristic height layers, lower stratosphere 15–35 km (LS), upper stratosphere 35–50 km (US), lower mesosphere 50–65 km (LM), and upper mesosphere 65–80 km (UM). —the bias μ (blue solid lines), the standard deviation σ (purple lines) of the bias and the 95% uncertainty range of the bias (blue dotted lines) of each layer are indicated, and estimated values given in the legend. (For interpretation of the references to color in this figure legend, the reader is referred to the web version of this article.)

the typical increase of error with solar activity, and the tendency for negative biases, are all well visible in Fig. 10. We

note that the biases are generally not statistically significant given the small number of data points averaged in the

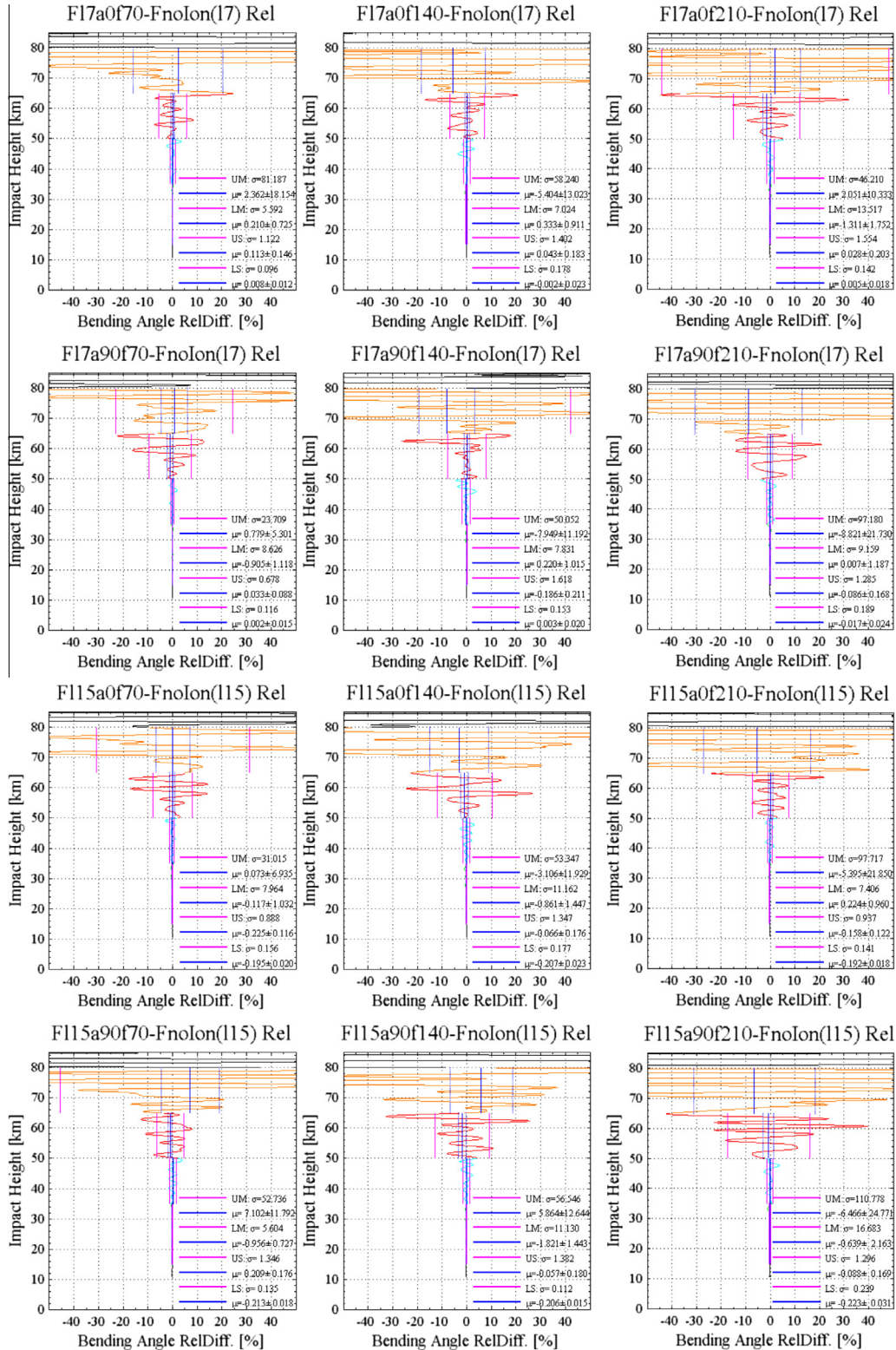


Fig. 9. Relative RIE profiles of the simulated bending angles and their statistical results over the same four characteristic height layers as shown in Fig. 8. —the layout is the same as in Fig. 8; the values in the legend are in units [%] here.

layers. Therefore uncertainty ranges are not graphically shown in order to avoid confusing Fig. 10; for uncertainty ranges see the legends in Fig. 8. More consolidated results need statistics from large ensembles of occultation events, which is left for future study.

The magnitude of bending angle RIEs found here can significantly affect the subsequent refractivity and atmospheric parameter retrievals and errors can be propagated downward to lower altitudes (Steiner and Kirchengast, 2005; Danzer et al., 2013), e.g., the lower stratosphere,

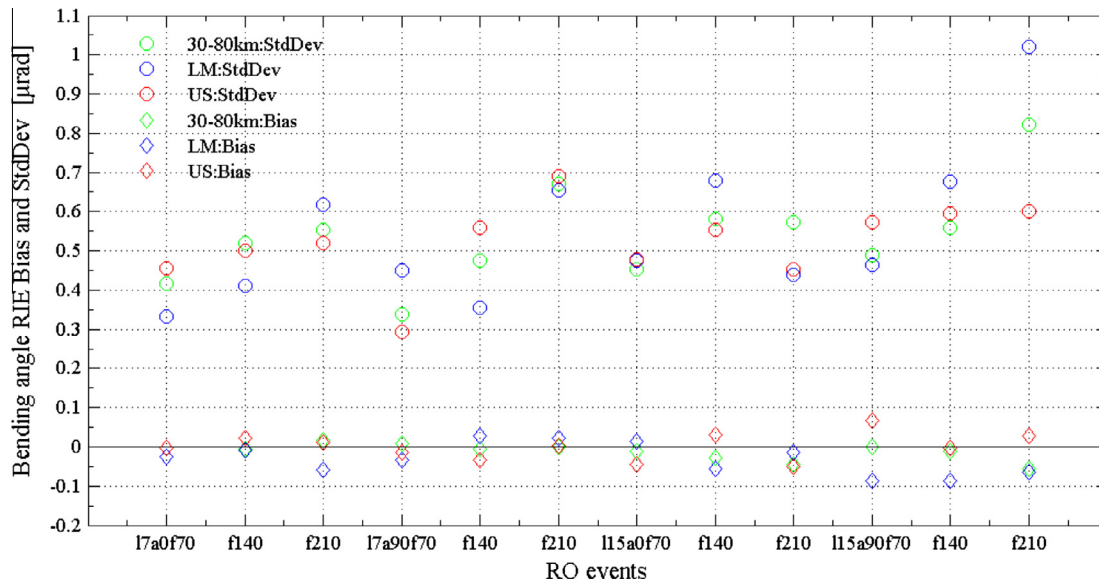


Fig. 10. Summary illustration of the values of biases (diamond symbols) and standard deviations (circle symbols) of the RIEs for the 12 RO events in the US (red), LM (blue), and 30–80 km impact height range (green), respectively. (For interpretation of the references to color in this figure legend, the reader is referred to the web version of this article.)

where atmospheric variable values are most important for NWP and climate applications (Steiner et al., 2011). As part of follow-on work we will quantitatively evaluate also the errors in subsequent refractivity and atmospheric profile retrievals. In closing this section, the effects of local time, solar intensity and RO plane direction on the RIEs are briefly discussed below.

4.4. The effects of local time

From Figs. 3–5, if comparing the two events at the same solar intensity level but in the two different locations, one can see that the VTEC (in Fig. 3) and electron density (in Figs. 4 and 5) at Location 2 are all significantly larger than that at Location 1. From Figs. 8 and 9, comparing the RIEs and the standard deviations of the two events that occurred at the same solar intensity levels and in the same direction but in the two different locations, we can find that most of the afternoon events had RIEs values greater than those of the morning events. While more statistics and bigger ensembles of events are needed for a robust picture, it is clear from these preliminary results already that daytime/afternoon events which find higher and more variable ionisation conditions have to be expected to be more vulnerable to RIEs. This is also in line with recent findings by Danzer et al. (2013) based on real RO data.

4.5. The effects of solar intensity

F10.7 is the most commonly used factor to represent the intensity of solar activity so it is a significant parameter in the NeUoG model used in the simulations. From Figs. 3–5 we can see significant differences of the VTEC and electron density between different ionisation levels due to different

solar activity intensities. Figs. 8 and 9 illustrate that most of the RIEs were greater at higher solar intensity than those at lower ones. This is in line with physical expectations and previous studies (Gobiet and Kirchengast, 2004); systematically higher electron densities at higher solar activities in average need to show up in RIEs – though also here more robust quantification based on a bigger ensemble of events will be useful as a next future step.

4.6. The effects of RO direction

TECs and electron density gradients along different directional RO ray paths are different. Comparing the results of the two ray paths at the same location and same ionisation level but in different directions in Figs. 4 and 5, we can see that at Location 1, the TEC and electron density gradient along the longitudinal ray paths are asymmetrical due to the night to day transition; at location 2, the TECs and electron density gradients along the latitudinal ray paths are asymmetrical due to the equatorial anomaly. As shown in Figs. 8 and 9, at Location 1, the longitudinal RIEs are generally larger than the latitudinal ones, but at Location 2 the longitudinal RIEs are generally less than the latitudinal ones. This indicates that the degree of asymmetry increases RIEs, which is sound, though also here better statistical quantification is needed in future.

All the above results indicate that local time and solar intensity are vital factors affecting the VTEC and electron density, which in turn affect the RIEs. The RO direction is also an important factor affecting the RIEs. The simulation results demonstrate that the RIEs in the afternoon events were greater than those of the morning events; the RIEs in higher solar activity were greater than those with

lower ones; and the RIEs under more asymmetric conditions tend to be higher.

5. Summary and conclusion

End-to-end simulations and a detailed single-event analysis of RIEs have been performed in this paper to investigate the characteristics of bending angle RIEs in the mesosphere and upper stratosphere. The results illustrate that the bending angle RIEs are significant in the mesosphere and upper stratosphere and their magnitude are affected by local time, the direction of RO planes and the intensity of solar activity. The RIEs are one of the main error sources of the bending angle, in MS and US, which need to be further characterised and potentially further mitigated for high-accuracy operational weather forecasting and climate monitoring applications, particularly under active space weather conditions.

As a next step we will look into bigger ensembles of events as well as at distinctly disturbed conditions to further quantify the behaviour of RIEs depending on the ionospheric state and its variability. The characterisation of the RIEs performed in this research is essential for the potential modelling of bending angle RIEs in future, which is expected to be highly valuable for ensuring benchmark-quality stratospheric RO data for applications like calibration/validation of other data sources and monitoring of climate change trends.

Acknowledgments

This research is partially supported by A Project Funded by the Priority Academic Program Development of Jiangsu Higher Education Institutions (PAPD) led by CUMT. The research at SPACE/RMIT is supported by the Australian Space Research Program (ASRP) and the Australian Research Council (ARC) (LP0883288) projects, the Australian Antarctic Division project (no. 4159) and the CAS/SAFEA International Partnership Program for Creative Research Teams (Grant No. KZZD-EW-TZ-05). The research at WEGC is supported by the European Space Agency (ESA) projects OPSGRAS and MMValRO.

References

- Bissiri, S., Hajj, G.A. High-order ionospheric effects on the GPS observables and means of modeling them. *Manuscr. Geodaet.* 18 (2), 280–289, 1993.
- Danzer, J., Scherllin-Pirscher, B., Foelsche, U. Systematic residual ionospheric errors in radio occultation data and a potential way to minimize them. *Atmos. Meas. Tech. Discuss.* 6, 1979–2008, 2013.
- Fjeldbo, G., Eshleman, V.R. The atmosphere of Mars analyzed by integral inversion of the Mariner IV occultation data. *Planet. Space Sci.* 16, 1035–1059, 1968.
- Foelsche, U., Pirscher, B., Borsche, M., Kirchengast, G., Wickert, J. Assessing the climate monitoring utility of radio occultation data: From CHAMP to FORMOSAT-3/COSMIC. *Terr. Atmos. Ocean. Sci.* 20, 155–170, 2009.
- Foelsche, U., Scherllin-Pirscher, B., Ladstädter, F., Steiner, A.K., Kirchengast, G. Refractivity and temperature climate records from multiple radio occultation satellites consistent within 0.05%. *Atmospheric Measurement Techniques* 4, 1593–1651, 2011.
- Fritzer, J., Kirchengast, G., Pock, M. End-to-end generic occultation performance simulation and processing system version 5.5 (EGOPS 5.5) Software User Manual, Tech. Rep. ESA-ESTEC WEGC-EGOPS-2011-TR01, Wegener Center and Inst. for Geophys., Astrophys., and Meteorol., Univ. of Graz, Austria., 2011.
- Gobiet, A., Kirchengast, G. Advancements of global navigation satellite system radio occultation retrieval in the upper stratosphere for optimal climate monitoring utility. *J. Geophys. Res.* 109 (D24110), 1–11, 2004.
- Gorbunov, M.E., Gurvich, A.S., Bengtsson, L. Advanced algorithms of inversion of GPS/MET satellite data and their application to reconstruction of temperature and humidity. Tech Rep.211, Max Plank Inst. for Meteorol. Hamburg, 1996.
- Hajj, G.A., Kursinski, E.R., Romans, L.J., et al. A technical description of atmospheric sounding by GPS occultation. *Atmos. Sol.-Terr. Phys.* 64, 451–469, 2002.
- Healy, S.B. Smoothing radio occultation bending angles above 40 km. *Ann. Geophys.* 19, 459–468, 2001.
- Hedin, A.E. Extension of the MSIS thermosphere model into the middle and lower atmosphere. *J. Geophys. Res.* 96 (A2), 1159–1172, 1991.
- Hoque, M.M., Jakowski, N. Higher order ionospheric propagation effects on GPS radio occultation signals. *Adv. Space Res.* 46 (2), 162–173, 2010.
- Kliore, A., Cain, D.L., Levy, G.S., et al. Occultation experiment: results of the first direct measurement of Mars's atmosphere and ionosphere. *Science* 149, 1243–1248, 1965.
- Kuo, Y.H., Schreiner, W.S., Wang, J., et al. Comparison of GPS radio occultation soundings with radiosondes. *Geophys. Res. Lett.* 32, 1–4, 2005.
- Kuo, Y.H., Sokolovskiy, S.V., Anthes, R.A., et al. Assimilation of GPS radio occultation data for numerical weather prediction. *Terr. Atmos. Ocean. Sci.* 11, 157–186, 2000.
- Kursinski, E.R., Hajj, G.A., Schofield, J.T., et al. Observing Earth's atmosphere with radio occultation measurements using the global positioning system. *J. Geophys. Res.* 102, 23429–23465, 1997.
- Lackner, B.C., Steiner, A.K., Hegerl, G.C., et al. Atmospheric climate change detection by radio occultation data using a fingerprinting method. *J. Clim.* 24, 5275–5291, 2011.
- Ladreiter, H.-P., Kirchengast, G. GPS/GLONASS sensing of the neutral atmosphere: model independent correction of ionospheric influences. *Radio Sci.* 31 (4), 877–891, 1996.
- Le, M.J., Xiao, Y., Norman, R., et al. The beneficial impact of radio occultation observations on Australian region forecasts. *Aust. Meteorol. Oceanogr. J.* 60, 121–125, 2010.
- Le, M.J., Xiao, Y., Norman, R., et al. The application of radio occultation observations for climate monitoring and numerical weather prediction in the Australian region. *Aust. Meteorol. Oceanogr. J.* 62, 323–334, 2012.
- Leitinger, R., Kirchengast, G. Easy to use global and regional models – a report on approached used in Graz. *Acta Geod. Geophys. Hung.* 32, 887–891, 1997.
- Leitinger, R., Titheridge, J.E., Kirchengast, G., et al. A simple global empirical model for the F layer of the ionosphere. *Kleinheubacher Berichte* 39, 679–704, 1996.
- Mannucci, A.J., Ao, C.O., Pi, X., Iijima, B.A. The impact of large scale ionospheric structure on radio occultation retrievals. *Atmos. Meas. Tech.* 4, 2837–2850, 2011.
- Melbourne, W.G., Davis, E.S., Duncan, C.B., et al. The application of spaceborne GPS to atmospheric limb sounding and global change monitoring. JPL Report, 1994 Jet Propulsion Lab/Calif. Inst. of Tech., Pasadena. pp. 94–18, 1994.
- Naidu, C.V., Durgalakshmi, K., Satyanarayana, G.C., et al. An observational evidence of climate change during global warming era. *Global Planet. Change* 79 (1–2), 11–19, 2011.

- Norman, R.J., Bennett, J.A., Dyson, P.L., et al. A ray-tracing technique for determining ray tubes in anisotropic media. *IEEE Antennas Propag. Soc.* 99, 1–13, 2013.
- Puviarasan, N., Giri, R.K., Ranalkar, M. Precipitable water vapour monitoring using ground based GPS system. *Mausam* 61, 203–212, 2011.
- Rieder, M.J., Kirchengast, G. Error analysis and characterization of atmospheric profiles retrieved from GNSS occultation data. *J. Geophys. Res.* 106 (D23), 29849–29866, 2001.
- Rocken, C., Anthes, R., Exner, M., et al. Analysis and validation of GPS/MET data in the neutral atmosphere. *J. Geophys. Res.* 102 (D25), 29849–29866, 1997.
- Scherllin-Pirscher, B., Steiner, A.K., Kirchengast, G., et al. Empirical analysis and modeling of errors of atmospheric profiles from GPS radio occultation. *Atmos. Meas. Tech.* 4 (2), 1875–1890, 2011.
- Steiner, A.K., Kirchengast, G. Error analysis for GNSS radio occultation data based on ensembles of profiles from end-to-end simulations. *J. Geophys. Res.* 110 (D15307), 1–21, 2005.
- Steiner, A.K., Kirchengast, G., Ladreiter, H.-P. Inversion, error analysis, and validation of GPS/MET occultation data. *Ann. Geophys.* 17, 122–138, 1999.
- Steiner, A.K., Lackner, B.C., Ladstädter, F., et al. GPS radio occultation for climate monitoring and change detection. *Radio Sci.* 46 (RS0D24), 1–17, 2011.
- Syndergaard, S. On the ionosphere calibration in GPS radio occultation measurements. *Radio Sci.* 35 (3), 865–883, 2000.
- Thies, B., Bendix, J. Satellite based remote sensing of weather and climate: recent achievements and future perspectives. *Meteorol. Appl.* 18, 262–295, 2011.
- Vorobev, V.V., Krasilnikova, T.G. Estimation of the accuracy of the atmospheric refractive index recovery from Doppler shift measurements at frequencies used in the NAVSTAR system. *Phys. Atmos. Ocean* 29, 602–609, 1994.
- Ware, R., Exner, M., Feng, D., et al. GPS sounding of the atmosphere from low earth orbit: preliminary results. *Bull. Am. Meteorol. Soc.* 77 (1), 19–40, 1996.